Infrared Vibrational Nanospectroscopy by Self-Referenced Interferometry

Benjamin Pollard,[†] Francisco C. B. Maia,[‡] Markus B. Raschke,[*,†] and Raul O. Freitas[*,‡]

[†]Department of Physics, Department of Chemistry, and Joint Institute for Lab Astrophysics (JILA), University of Colorado, Boulder, Colorado 80309, United States

[‡]Brazilian Synchrotron Light Laboratory, Campinas, 13083-100 São Paulo, Brazil

S *Supporting Information*

ABSTRACT: Infrared vibrational scattering scanning near-field optical microscopy (*s*-SNOM) has emerged as a new frontier in imaging science due to its potential to provide nanoscale spatially resolved chemical spectroscopy for the investigation of molecular, soft-matter, and biological materials. As a phase-sensitive technique able to yield the full complex dielectric function of materials, different interferometric schemes have been developed involving asymmetric interferometry between sample and reference arms. In this work, we take advantage of a greatly simplified symmetric geometry that uses the spatially coherent background scattered light from within the confocal sample volume as a reference field for signal amplification in both self-homodyne and self-heterodyne interferometry. On the basis of a simple model for tip–sample scattering and interferometric detection, we demonstrate the measurement of the vibrational response of molecular materials in good agreement with established values. In addition to a compact design, enhanced signal levels, and a reduced sensitivity to fluctuations and drift, including those from the light source, self-referenced interferometry brings benefits for routine *s*-SNOM chemical spectroscopy, remaining robust even under a wide range of challenging experimental environments.

KEYWORDS: nano-FTIR, nanoscale molecular fingerprint, infrared nanospectroscopy, self-homodyne/self-heterodyne detection, self-referenced interferometry
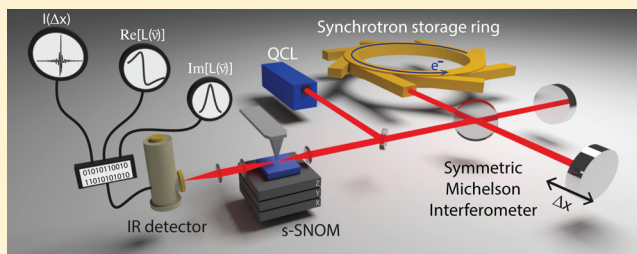
As a nanoscale analog of conventional infrared (IR) vibrational spectroscopy,[1,2] infrared vibrational scattering scanning near-field optical microscopy (*s*-SNOM)[3–6] is a powerful tool for obtaining nanospectroscopic insight into a wide range of materials,[7–10] including protein complexes,[11] chemical identification of nanoscale domains of mixed polymers,[12] chemical mapping of biominerals,[13] and coherent ultrafast vibrational spectroscopy.[14] For details, see reviews and references therein.[15–17] Achieved with both tunable IR laser systems and broadband-source Fourier transform infrared spectroscopy (FTIR) schemes, *s*-SNOM spectra yield, to a good approximation, the extinction coefficient $\kappa(\bar{\nu})$ and consequently the infrared absorption spectrum of a nanometer-sized region of the material.[12]

Most *s*-SNOM spectroscopic techniques established to date are based on an asymmetric Michelson interferometer, aiming to provide spectra of the complex index of refraction $\tilde{n}(\bar{\nu})$ of the sample. Different interferometric techniques have been developed for the phase sensitive detection of the weak near-field tip-scattered field of interest $\tilde{E}_{nf}$ by phase modulation and control of a reference field $\tilde{E}_{ref}$[12,18–20] in conjunction with signal demodulation at higher harmonics of the Atomic Force Microscope (AFM) cantilever motion. In typical *s*-SNOM measurements, $\tilde{E}_{nf} = E_{nf}e^{i\phi}$ experiences amplified interference with both a far-field background $\tilde{E}_{ff} = E_{ff}e^{i\theta}$ of uncontrolled

phase θ scattered by the tip and/or sample, and with reference arm field $\tilde{E}_{ref} = E_{ref}e^{i\phi_{ref}}$ of controlled phase ϕ_{ref} when the AFM setup is part of an asymmetric Michelson interferometer. As a result, the total demodulated signal intensity detected with an asymmetric setup is dominated by $I_{as} \propto E_{nf}E_{ref}e^{i(\phi-\phi_{ref})} + E_{nf}E_{ff}e^{i(\phi-\theta)}$. Much work in *s*-SNOM has aimed at eliminating the term containing E_{ff} from the detected signal, as it has been treated only as a source of artifacts with no useful information due to its uncontrolled phase.[18] Furthermore, the underlying asymmetric *s*-SNOM geometry requires the AFM to be located in one of the arms of the interferometer (sample arm) which is typically few to several tens of centimeters long, depending on experimental constraints. As a consequence, the sample arm must operate with interferometric stability, overcoming signal fluctuations associated with small beam misalignments and atmospheric IR absorption over long path lengths. Although active interferometer stabilization and dry nitrogen/air purging may address these limitations, they add considerable experimental complexity.

Here, we present a simplified approach to *s*-SNOM nanospectroscopy based on a symmetric optical detection

scheme. It uses the otherwise suppressed background field $\tilde{E}_{ff}$ as a local reference field in two modalities: self-homodyne s-SNOM with a narrow-band continuous wave (CW) laser and self-heterodyne broadband s-SNOM, including synchrotron infrared nanospectroscopy (SINS). Although spatially coherent under a confocal illumination and detection geometry, $\tilde{E}_{ff}$ has an unspecified phase emerging from spatially distributed scatterers within the confocal volume, that is, the region of illuminated space at the sample surface. Similar to other techniques that require consideration of an unknown reference phase, including NMR,[21] SFG,[22,23] X-ray diffraction,[24,25] and Raman[26] spectroscopies, self-referenced interferometry involves incorporating certain a priori knowledge about the spectral behavior of the underlying system to overcome the phase retrieval problem. We propose a simple self-referenced interferometry model (SRIM) that incorporates $\tilde{E}_{ff}$ of unknown but fixed phase and assumes a defined spectral line shape function to describe molecular vibrational modes. Using SRIM, we accurately determine the vibrational spectral line shape of the real and imaginary parts of the s-SNOM signal, with peak position and line shape in agreement with the complex refractive index measured via far-field spectroscopic ellipsometry. This approach allows for vibrational spectroscopic material identification with nanoscale spatial resolution using self-heterodyne SINS or self-homodyne s-SNOM spectroscopy. We demonstrate the performance of our technique on a range of characteristic vibrational modes of molecular and soft matter.

Our method is particularly attractive for s-SNOM with lasers exhibiting high levels of phase noise, mode hopping, and instability on second to millisecond time scales, as well as for SINS. Benefiting from high spectral irradiance, spatial coherence, and extended source bandwidth, SINS has successfully been applied in the nanoscale characterization of semiconductors[27] and the chemical identification of biominerals and proteins.[28] Despite the presence of many noise sources in large experimental facilities accommodating an electron storage ring,[29,30] self-heterodyne SINS remains a sensitive and robust tool for identifying resonant signatures in a variety of materials such as semiconductors, polymers, and proteins.

Methods and Experiment. Tunable CW laser s-SNOM spectroscopy measurements were performed at the University of Colorado Boulder using a standard s-SNOM setup, similar to ref 31, presented in Figure 1a, which was capable of performing all standard s-SNOM detection modalities. IR radiation generated from a quantum cascade laser (QCL, Daylight Solutions), tunable between 1660 and 1900 cm^{-1}, was focused onto the apex of an AFM tip (PtSi-NCH, NanoWorld AG) in a modified AFM (MultiMode 8, Bruker) using a 0.45 NA off-axis parabolic mirror, and then detected with a mercury cadmium telluride (MCT) detector (MCT KLD-0.2S, Kolmar Technologies Inc.) using third harmonic lock-in amplification (HF2LI, Zurich Instruments). The reference arm was blocked for self-homodyne detection.

SINS measurements were performed at the Brazilian Synchrotron Light Laboratory (Laboratório Nacional de Luz Síncrotron, LNLS), using IR synchrotron radiation with beam extraction and optics described in ref 32. The synchrotron source delivers radiation from THz to near-IR with improved spectral irradiance compared to thermal sources[33] (Figure 1c). As shown in Figure 1b, the collimated IR synchrotron beam first passes through a symmetric Michelson interferometer which contains a ZnSe beamsplitter and a piezo linear stage (P.629.1 PIHera, Physik Instrumente GmbH & Co.). All SINS
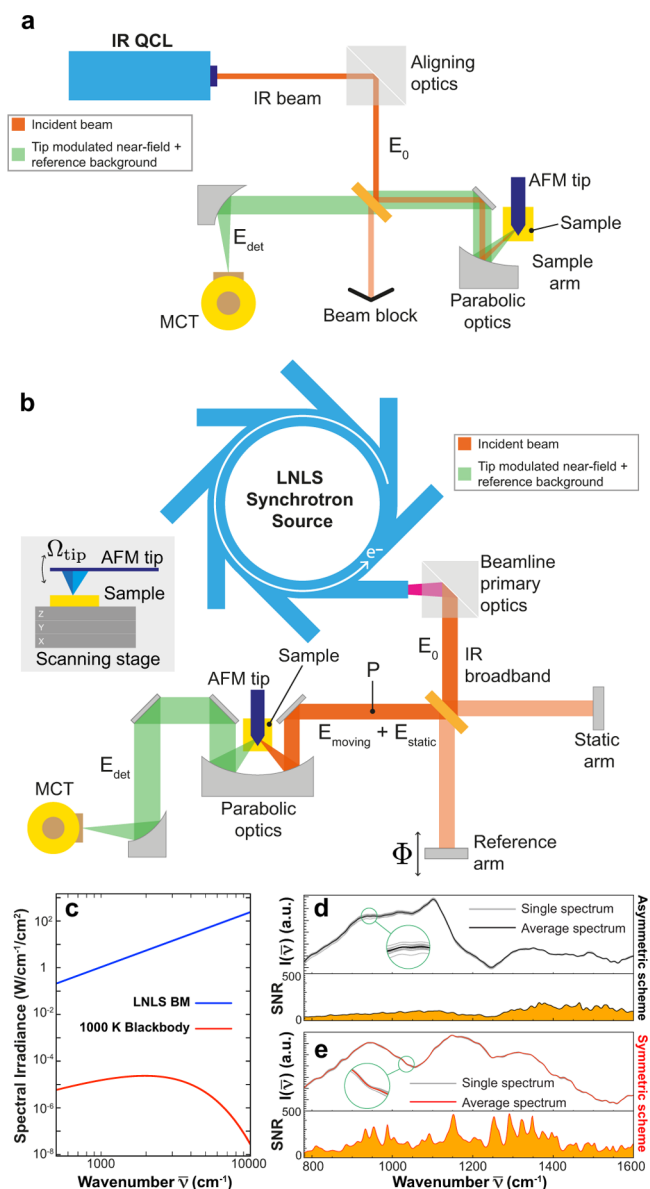
Figure 1. (a) Self-homodyne s-SNOM optical scheme using a tunable single-frequency laser source. (b) Self-heterodyne SINS endstation in the IR1 beamline of LNLS. (c) Calculated spectral irradiance of the LNLS IR1 beamline (bending magnet radiation) and typical 1000 K thermal source (blackbody radiation) for comparison. Both synchrotron and blackbody spectral irradiances were calculated using X-ray oriented programs (XOP). (d–e) Sample raw spectra on Au taken with an asymmetric SINS setup (d) and self-heterodyne SINS (e). Measurements were repeated (gray) and averaged (black/red) to illustrate the improved stability of the symmetric configuration, which is further quantified in plots of signal-to-noise ratio (SNR) below each set of spectra.

experiments in this paper were taken with 6.5 cm^{-1} spectral resolution. Spectra were acquired by scanning the reference mirror at a rate of 20 μm/s. IR broadband images were taken at typical 1 μm/s AFM scanning rates. The collinearly recombined beams then enter a commercial s-SNOM microscope (NeaSNOM, Neaspec GmbH), where they are focused onto the apex of an AFM tip (PtSi-NCH, NanoWorld AG) using a 0.45 NA off-axis parabolic mirror. Both beams exiting the symmetric interferometer produce near-field signal. Forward-scattered light from the tip-mediated near-field

interaction is detected using an MCT detector (MCT KLD-0.1, Kolmar Technologies Inc.) with sensitivity spanning 700−5000 cm^{-1}. The self-heterodyne SINS signal was extracted via second harmonic lock-in demodulation following established s-SNOM procedures.[16,34,35]

A direct comparison between asymmetric (Figure S1) and symmetric (Figure 1b) schemes is shown in Figure 1d−e (for more detail, see Supporting Information). Eleven raw spectra (gray lines) on a Au surface were taken in sequence using each scheme, and then averaged (black/red lines). We define the signal-to-noise ratio (SNR) at each wavenumber as the inverse of the coefficient of variation and calculate SNR by taking the ratio of the average signal to the standard deviation within the sequence. Less variation between spectra is apparent in the symmetric data, yielding an overall 87% improvement in SNR over the asymmetric setup when integrated over the spectral range. Differences in the overall spectral shape between Figure 1d and e are a result of differences in optical alignment and do not affect the comparison of SNR. All other spectra in this work are normalized to a corresponding nonresonant reference spectrum for the respective setup to remove the inherent instrument response function.

Attenuated total reflectance (ATR) FTIR and ellipsometry setups used for far-field comparison are described in the Supporting Information.

Results. We first address self-heterodyne SINS on a rectangular SiO$_2$/Si microstructure (TGQ1, NT-MDT Co). Figure 2a,b show AFM topography and broadband IR images of the microstructure, respectively. Surface profiles corresponding to the dashed lines traced on Figure 2a−b are plotted in Figure
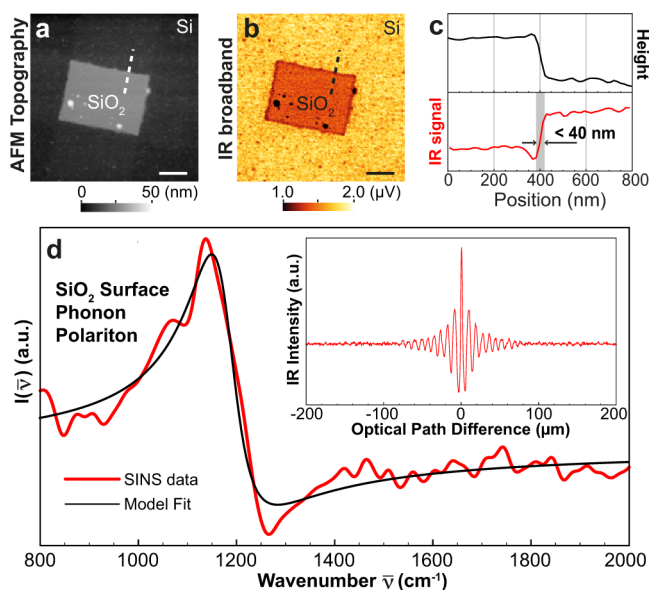
Figure 2. Self-heterodyne SINS and IR broadband imaging of SiO$_2$ micropattern on Si. AFM topography (a) and IR broadband image (b) simultaneously recorded. (c) AFM height and IR signal along the dashed lines in (a) and (b) (SiO$_2$−Si step) confirming that the SINS spatial resolution is comparable to AFM (<40 nm in this case). (d) SINS broadband spectrum of SiO$_2$/Si (red) and the respective SRIM fit (black) as described below. To account for the discrepancies in the spectral intensity due to the system responsivity, the SiO$_2$ SINS spectrum has been normalized to the Si substrate SINS spectrum. Symmetric interferogram (inset) acquired using the self-heterodyne detection scheme described in Figure 1b. Scale bars in (a) and (b) represent 500 nm.

2c. The plateau in AFM topography is the 30 nm high SiO$_2$ layer, with correspondingly low optical signal due to the reduced infrared scattering of SiO$_2$. The 40 nm lateral SiO$_2$−Si boundary is optically resolved and the surface profiles in Figure 2c confirm optical resolution comparable to AFM. Self-heterodyne SINS on a nanodomain of the SiO$_2$ microstructure yields the symmetric interferogram (inset of the Figure 2d) and the corresponding spectrum shown in Figure 2d. The strong feature at 1137 cm^{-1}, associated with the surface phonon polariton mode (SPhP), occurs at the same spectral location as the corresponding peak measured with an asymmetric SINS setup.[27,28]

We further investigate an 80 nm thick poly(methyl methacrylate) (PMMA) film on a Au substrate, as an example of a local molecular vibrational oscillator. AFM topography and self-heterodyne IR images around a hole formed in the PMMA film due to solvent evaporation are presented in Figure 3a−b.
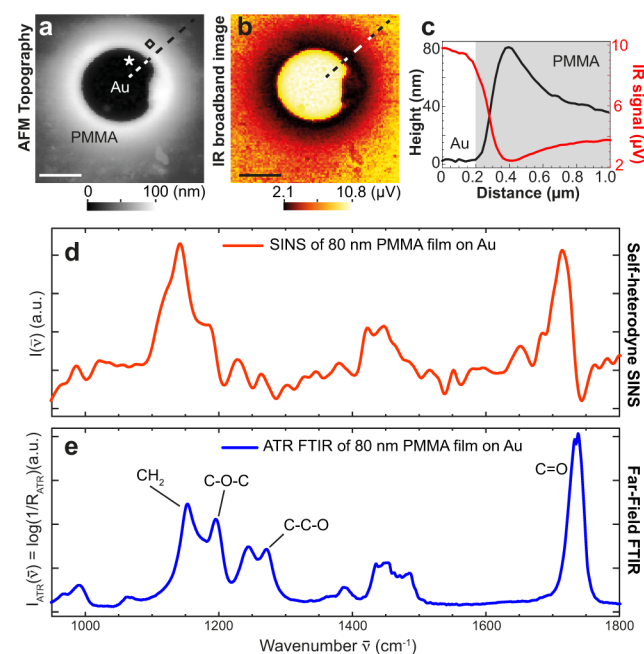
Figure 3. Self-heterodyne SINS and IR broadband imaging of PMMA microcrater on Au. AFM topography (a) and IR broadband image (b) of a micrometer size crater-like structure formed by PMMA spin-coated on Au substrate. The center rounded feature (lower topography and higher optical signal) denotes the exposed Au substrate. (c) Topography and SINS intensity profiles along the dashed line in (a) and (b) showing the relation of the IR broadband signal with the thickness of the PMMA film. (d) Self-heterodyne SINS taken on the PMMA (◇ mark) normalized by a reference spectrum taken on Au (★ mark). (e) Macroscopic far-field ATR-FTIR absorbance of the same PMMA/Au sample measured in (a)−(d). Scale bars in (a) and (b) represent 500 nm.

Figure 3c shows AFM and IR signal profiles along the dashed lines illustrated in Figure 3a−b. AFM and IR signals correlate inversely indicating film thickness dependence, with optical resolution comparable to AFM. Figure 3d shows a self-heterodyne SINS spectrum of PMMA obtained at the ◇ region normalized to a Au reference spectrum measured at ★. Figure 3e presents a far-field absorption spectrum of the same sample produced by convetional ATR FTIR, with the molecular absorption lines of PMMA around 1145 cm^{-1} (CH$_2$ bending), 1190 cm^{-1} (C—O—C bending), 1265 and

1240 cm^{-1} (C—C—O stretching), and 1730 cm^{-1} (C=O stretching).[12] Consistently, the self-heterodyne SINS spectrum presents similar vibrational features compared to the ATR FTIR spectrum (Figure 3e), again showing a semidispersive line shape as was the case for the SiO$_2$ SPhP mode. In the following, we present a model that accounts for this line shape variation and allows for the extraction of optical properties from self-referenced interferometry.

Self-Referenced Interferometry: Concept and Modeling. Several models[36−40] have been developed to describe the s-SNOM scattered field from a tip-mediated near-field interaction, with varying levels of complexity and accuracy. Irrespective of the particular model used, the coupled tip−sample system can be expressed in terms of a complex effective polarizability $\alpha = Ae^{i\phi}$, which is directly proportional to the near-field-scattered electric field. In our symmetric interferometer configuration, this field is detected through interferometric amplification with other scattered fields from the confocal volume but independent of the tip−sample interaction. Often called "far-field scattering" in s-SNOM, these other scattered fields are expressed as $r = Re^{i\theta}$. We assume here that the resulting far-field background is dominated by scattering from the tip and nonresonant surface defects, as is the case in most IR s-SNOM experiments, and thus is spectrally flatter than a purely resonant near-field response over the spectral region of interest. Therefore, it can be shown (see Supporting Information), both for self-homodyne (Figure 1a) and self-heterodyne (Figure 1b) setups, that the resulting detected intensity I is given by

$$I(\bar{\nu}) = 2|E_0|^2 RA(\bar{\nu})\cos(\phi(\bar{\nu}) - \theta) \qquad (1)$$

where $|E_0|^2$ is the incident intensity.

Although coherent and well-defined at a given tip location, the far-field phase θ in eq 1 is unknown, resulting in uncontrolled line shape variation of $I(\bar{\nu})$. This variation can be visualized by separating the nonresonant and resonant contributions, as shown in Figure 4a. The nonresonant contribution differs from the local reference field by θ, whereas the resonant near-field contribution acquires a phase ϕ. Using a Lorentzian resonance for example, the resonant response traces out a circle in the complex plane as shown in Figure 4b. $I(\bar{\nu})$ is proportional to $A(\bar{\nu}) \cos(\phi(\bar{\nu}) - \theta)$, labeled as x in Figure 4b. Depending on the value of θ, the resulting spectral lineshapes (Figure 4c) can be entirely dispersive, entirely absorptive, or a corresponding combination. By fitting an experimental profile $I(\bar{\nu})$, however, we can extract the underlying parameters, including θ, and reconstruct the line shape of a conventional spectroscopic measurement of, for example, absorption.

Applying this self-referenced interferometry model (SRIM) to a Lorentzian sample response

$$L(\bar{\nu}) = \sum_{j=1}^{N} a_j L_j(\bar{\nu}) + C = \sum_{j=1}^{N} a_j \left(\frac{\bar{\nu}\Gamma_j}{\bar{\nu}_{0,j}^2 - \bar{\nu}^2 - i\bar{\nu}\Gamma_j} \right) + C \qquad (2)$$

with a real-valued, nonresonant contribution C, we set $A(\bar{\nu}) = |L(\bar{\nu})|$ and $\phi(\bar{\nu}) = \text{Arg}[L(\bar{\nu})]$. For a set of N resonances, $L(\bar{\nu})$ is a combination of individual resonators j, with scaling factors a_j, which can carry information on local molecular order through the relative resonator intensities. eq 1 then yields a fitting function for $I(\bar{\nu})$ as

$$I(\bar{\nu}) = R|L(\bar{\nu})|\cos(\text{Arg}[L(\bar{\nu})] - \theta) \qquad (3)$$
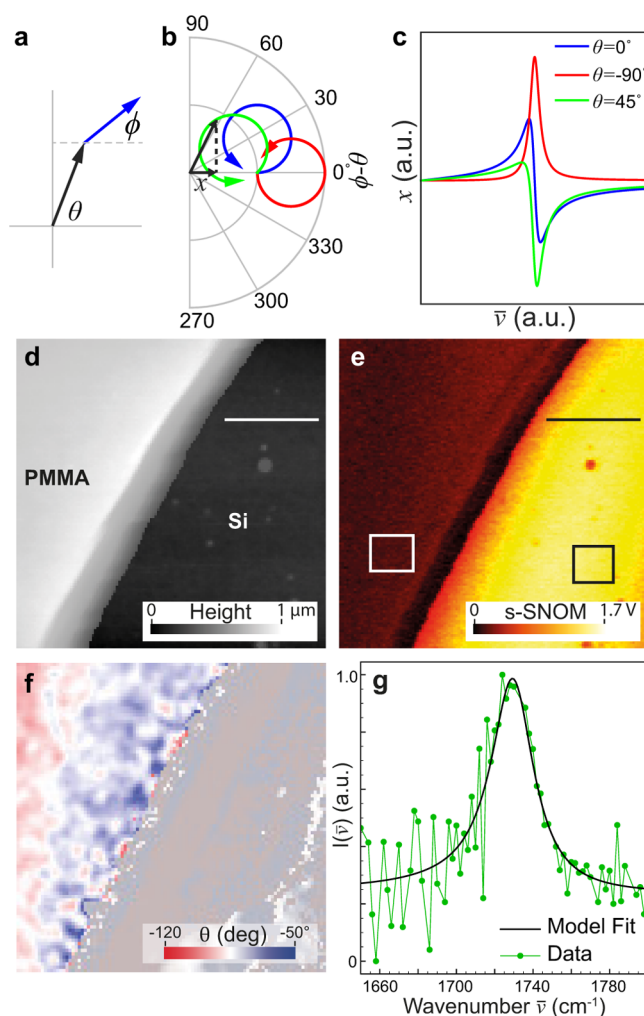
Figure 4. Effect of the reference phase θ in self-referenced interferometry. (a) Relation between resonant (blue) and nonresonant (black) contributions to the complex sample response. (b) Polar representation of the complex sample response, traced out as a parametric function of ν, for different far-field phases θ. (c) Resulting spectral shapes proportional to $I(\bar{\nu})$ for far-field phases $\theta = 0°$, $\theta = -90°$ and $\theta = 45°$. (d) AFM topography and (e) single-frequency on-resonance self-homodyne s-SNOM map of PMMA layer on Si substrate (scale bar 1 μm). Using the silicon region (inside black rectangle) shown in (e) as a reference, spectral fits to eq 3 were performed at every pixel. (f) Spatial map of far-field phase θ from the spectral fits, with the nonresonant Si region grayed out for visual clarity, showing an overall change in the far-field phase over wavelength-scale distances from the step edge. (g) Self-homodyne s-SNOM spectrum from PMMA region (inside white rectangle) shown in (e), with corresponding model fitting.

with free parameters $\bar{\nu}_{0,j}$ (peak position), Γ_j (line width), C (nonresonant response), θ (far-field phase), and R (scaling factor). The incident field E_0 is treated as a single scaling factor included in the far-field amplitudes R with arbitrary units.

We verify this model using self-homodyne s-SNOM on a PMMA-Si step edge. Figure 4d−e shows AFM and IR s-SNOM maps measured with the self-homodyne QCL s-SNOM setup illustrated in Figure 1a. A spatiospectral data set across the C=O stretch band was produced from this region, as discussed in ref 31, with fits to eq 3 performed at every pixel. A sample self-referenced spectrum is presented in Figure 4g from the regions marked in e (white and black rectangles), with respective fit. A

spatial map of the obtained values of the far-field phase θ is shown in Figure 4f, displaying a gradual retardation with increasing distance from the PMMA edge on the order of the wavelength (~6 μm) due to propagation delays. The finer spatial heterogeneity observed in θ arises from the combined interference of multiple scattering centers along the edge and other reference inhomogeneities due to the precise geometry of incident and scattered wave fronts changing with tip position. The dominance of the PMMA edge in our measured θ illustrates that the technique properly accounts for far-field amplification and interference and supports the validity of parametrizing self-homodyne/self-heterodyne spectra with a single far-field phase.

Further analysis was performed on spectra from a PMMA film to compare the results of SINS and QCL s-SNOM self-referenced interferometry to established techniques. In Figure 5a, self-heterodyne SINS spectra are fit to eq 3. Figure 5b shows a conventional amplitude s-SNOM spectrum of PMMA measured using an asymmetric detection scheme identical to that employed in ref 31. For comparison, Figure 5b also shows the amplitude spectrum $|L(\nu)|$ based on the model parameters obtained from the fit in Figure 4g. Figure 5c−d shows comparisons between the spectra extracted from self-heterodyne SINS, self-homodyne QCL s-SNOM, and far-field spectral ellipsometry. The good agreement between these spectra illustrates that the complex-valued response extracted from the SRIM is compatible with conventional s-SNOM measurements. Moreover, when compared to far-field ellipsometry and ATR-FTIR, the spectra determined via self-referenced interferometry present good agreement in line width and peak position with the extinction coefficient κ and/or absorption, to within the 6.5 cm^{-1} spectral resolution of our measurement. Slight variations in line shape, at a level also not uncommon when comparing between conventional far-field infrared spectroscopic techniques such as FTIR, could perhaps result from tip−sample coupling, which typically results in <1 cm^{-1} shifts for vibrational resonances.[17]

The approach can readily be extended to also include different models to treat the tip−sample interaction, which are a continuing focus in s-SNOM development.[40−42] For example, using the finite dipole model (FDM) from ref 38, we formulate the complex coupled response of the tip−sample system to replace $L(\bar{\nu})$ in eq 3, and then employ this new equation to fit self-heterodyne SINS spectra (see Supporting Information). In Figure 6a, we present a self-heterodyne SINS broadband spectrum of an 80 nm film of poly(dimethylsiloxane) (PDMS) on Au, and fit the Si-CH$_3$ vibrational band in PDMS (Figure 6b) both with a Lorentzian directly and by incorporating the FDM. We compare spectra calculated from our model fit to the corresponding ATR FTIR band (see Figure 6c−d), showing satisfactory agreement of the resonance position within the spectral resolution of the SINS experiment.

We also applied self-reference interferometry to study a variety of vibrational modes and multiple resonances simultaneously. Figure 7a−b shows previously published self-referenced QCL spectra of 1,3,5-trinitroperhydro-1,3,5-triazine (RDX) and pentaerythritol tetranitrate (PETN) (data from ref 43) with corresponding fits to eq 3. From the fit parameters, we plot the respective extracted SRIM spectra in Figure 7d−e. Such model-defined resonant frequencies are consistent with previous reports on those molecules and point to peak positions around 1314 cm^{-1} (symmetric nitro stretch)[44] for RDX and to two resonances for PETN, around 1271 and 1285
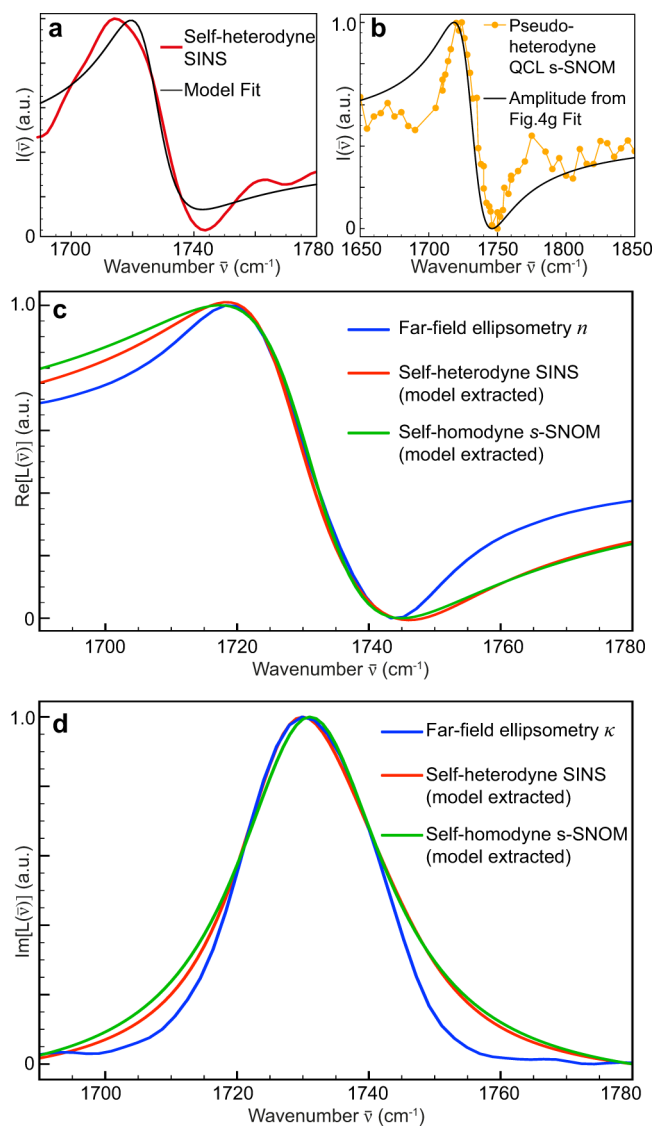
Figure 5. PMMA IR spectra extracted from self-referenced SINS and QCL s-SNOM data. (a) SINS self-heterodyne spectrum from PMMA film around the C═O stretching band, with spectral fit to the eq 3. (b) C═O stretching band of PMMA measured with a QCL in a typical pseudoheterodyne detection scheme. For comparison, the near-field amplitude $A(\bar{\nu})$, extracted from the fitting in Figure 4g, is also plotted (black line). (c) Real and (d) imaginary components of PMMA spectra extracted from both SINS and QCL s-SNOM self-referenced schemes, all normalized between zero and one for comparison with n and κ, respectively, from far-field spectral ellipsometry.

cm^{-1} (hybridized C—H bends, nitro stretches, and skeletal modes).[45] Finally, a similar treatment has been performed for bovine serum albumin BSA on Au (Figure 7c−f), observed in previous work using asymmetric SINS,[28] that shows the vibrational modes attributed to Amide I (1620 cm^{-1} to 1700 cm^{-1}) and Amide II (1500 cm^{-1} to 1560 cm^{-1}). Two resonances were used to fit the two modes in the PETN spectrum with a phase difference of $\Theta = 35$ deg between them. Three resonances were used to fit the BSA due to a splitting of the Amide I peak.

Discussion and Conclusion. The experimental results above, as analyzed by the SRIM, show that accurate intrinsic sample spectral properties can be determined from self-
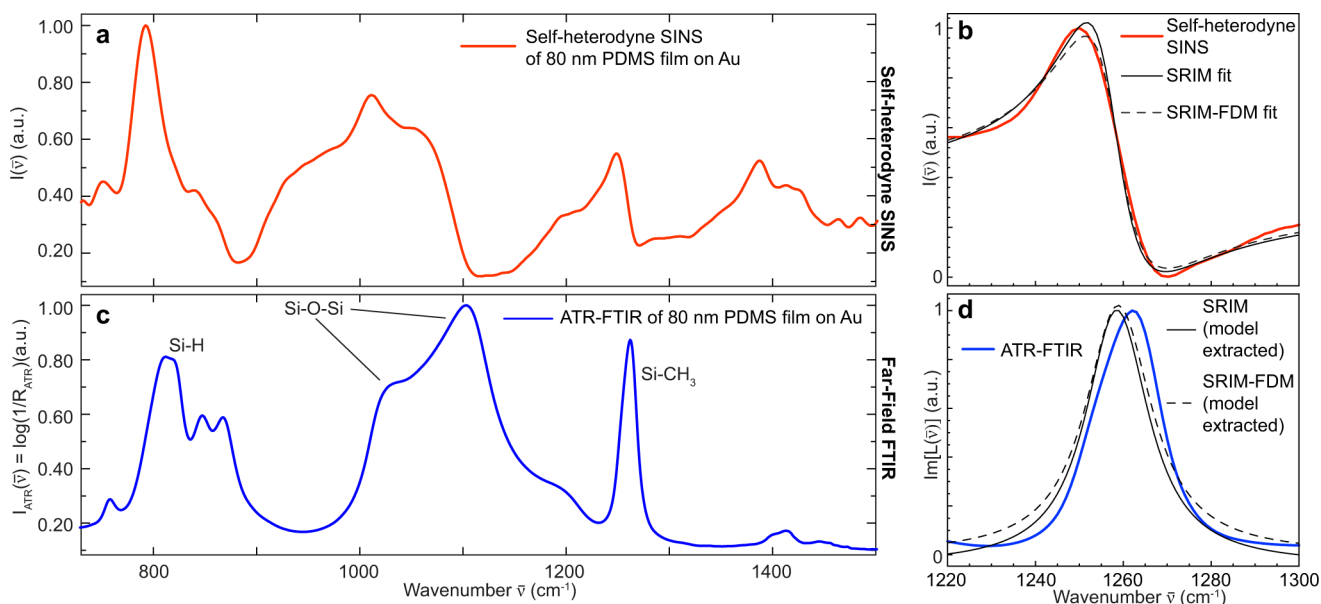
Figure 6. Near-field spectra of PDMS/Au film extracted from self-heterodyne SINS data compared to far-field FTIR, normalized as in Figure 5. (a) Self-heterodyne SINS spectrum of 80 nm PDMS/Au film normalized by Au reference spectrum. (b) SRIM fits, using both a Lorentzian directly and the combined SRIM-FDM, of the PDMS Si-CH$_3$ symmetric deformation band using eq 3. (c) ATR-FTIR absorbance of the same PDMS/Au film showing molecular fingerprints in the measured range. The spectrum reveals the characteristic vibrational resonances of PDMS around 810 cm^{-1} (Si—H deformation), 1040 and 1100 cm^{-1} (Si—O—Si asymmetric stretching), and 1270 cm^{-1} (Si—CH$_3$ symmetric deformation).[12] (d) Near-field spectra extracted from the model fits in (b) compared to the far-field absorbance.
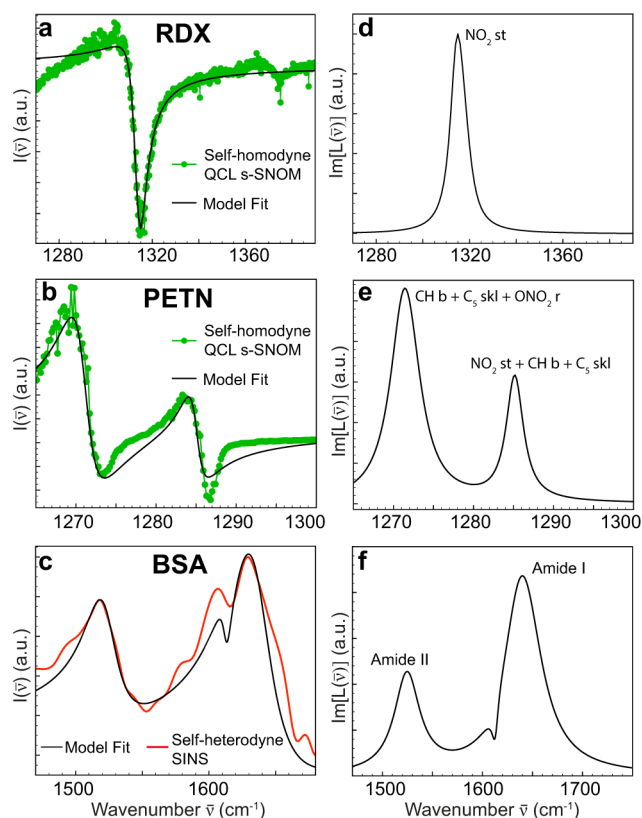
Figure 7. Self-homodyne QCL s-SNOM and SINS spectra and model fittings of explosive polymers RDX (a), PETN (b), and bovine protein BSA (c). (d)−(f) Extracted near-field spectra from SRIM analysis of (a)−(c), respectively. Data in (a)−(b) from ref 43.

homodyne or self-heterodyne *s*-SNOM and SINS. Despite the computational complexity, the model is not overparameterized

and the fit results are robust provided sufficient signal-to-noise ratio, as verified by the range of material systems analyzed here. Furthermore, the SRIM can in principle be combined with other established tip-sample interaction models (like the FDM), allowing self-homodyne or self-heterodyne nano-spectroscopy to yield the same information regularly obtained using those models, including quantitative optical constants in certain cases.

The primary benefit of performing self-homodyne spectros-copy or self-heterodyne SINS is increased stability due to reduced sensitivity to fluctuations and drift, leading to shorter measurement times and more robust data collection. Greater simplicity in the optical setup is also achieved by completely decoupling the interferometer from the microscope, as is common in far-field FTIR microscopy. Other benefits are also made possible by this decoupling, such as different pathways for the incoming and outgoing light using separate illumination and collection optics.

In summary, we have introduced self-referenced interferom-etry as a conceptually simple and robust approach for investigating vibrational signatures of materials. The suggested detection scheme uses the omnipresent far-field scattering $\tilde{E}_{ff}$ from the *s*-SNOM confocal volume as a reference for nanoscale resolved interferometry. We demonstrated that $\tilde{E}_{ff}$ can serve as a reliable reference for near-field amplification and spectrosco-py. In vibrational analysis, direct examination of self-referenced spectra matches qualitatively with standard spectra produced by traditional far-field techniques, and modeling using SRIM allows for the extraction of a material's vibrational spectroscopic response with nanoscale spatial resolution.

ASSOCIATED CONTENT

Supporting Information

The Supporting Information is available free of charge on the ACS Publications website at DOI: 10.1021/acs.nano-lett.5b02730.

Experimental procedures, data treatment details, and fitting parameters are presented. (PDF)

AUTHOR INFORMATION

Corresponding Authors
*E-mail: markus.raschke@colorado.edu.
*E-mail: raul.freitas@lnls.br.

Notes
The authors declare no competing financial interest.

ACKNOWLEDGMENTS

REFERENCES

(1) Griffiths, P. R.; Haseth, J. A. *Fourier Transform Infrared Spectrometry*, 2nd ed.; Wiley-Interscience: Weinheim, Germany, 2007.

(2) Bell, R. J. *Introduction to Fourier Transform Spectroscopy*, 2nd ed.; Academic Press: Waltham, MA, 1972.

(3) Zenhausern, F.; Martin, Y.; Wickramasinghe, H. K. *Science* **1995**, *269*, 1083−1085.

(4) Knoll, B.; Keilmann, F. *Nature* **1999**, *399*, 134−137.

(5) Kawata, S.; Inouye, Y. *Ultramicroscopy* **1995**, *57*, 313−317.

(6) Bachelot, R.; Gleyzes, P.; Boccara, A. C. *Opt. Lett.* **1995**, *20*, 1924−1926.

(7) Huber, A.; Ocelic, N.; Taubner, T.; Hillenbrand, R. *Nano Lett.* **2006**, *6*, 774−778. PMID: 16608282.

(8) Di Florio, G.; Bründermann, E.; Yadavalli, N. S.; Santer, S.; Havenith, M. *Soft Matter* **2014**, *10*, 1544−54.

(9) Dai, S.; et al. *Nat. Nanotechnol.* **2015**, *10*, 682−6.

(10) Khatib, O.; Wood, J. D.; McLeod, A. S.; Goldflam, M. D.; Wagner, M.; Damhorst, G. L.; Koepke, J. C.; Doidge, G. P.; Rangarajan, A.; Bashir, R.; Pop, E.; Lyding, J. W.; Thiemens, M. H.; Keilmann, F.; Basov, D. N. *ACS Nano* **2015**, *9*, 7968−75.

(11) Amenabar, I.; Poly, S.; Nuansing, W.; Hubrich, E. H.; Govyadinov, A. A.; Huth, F.; Krutokhvostov, R.; Zhang, L.; Knez, M.; Heberle, J.; Bittner, A. M.; Hillenbrand, R. *Nat. Commun.* **2013**, *4*, 2890.

(12) Huth, F.; Govyadinov, A.; Amarie, S.; Nuansing, W.; Keilmann, F.; Hillenbrand, R. *Nano Lett.* **2012**, *12*, 3973−3978.

(13) Amarie, S.; Zaslansky, P.; Kajihara, Y.; Griesshaber, E.; Schmahl, W. W.; Keilmann, F. *Beilstein J. Nanotechnol.* **2012**, *3*, 312−323.

(14) Atkin, J. M.; Sass, P. M.; Teichen, P. E.; Eaves, J. D.; Raschke, M. B. *J. Phys. Chem. Lett.* **2015**, *6*, 4616.

(15) Bründermann, E.; Havenith, M. *Annu. Rep. Prog. Chem., Sect. C: Phys. Chem.* **2008**, *104*, 235.

(16) Keilmann, F.; Hillenbrand, R. *Philos. Trans. R. Soc., A* **2004**, *362*, 787−805.

(17) Muller, E. A.; Pollard, B.; Raschke, M. B. *J. Phys. Chem. Lett.* **2015**, *6*, 1275−1284.

(18) Ocelic, N.; Huber, A.; Hillenbrand, R. *Appl. Phys. Lett.* **2006**, *89*, 101124.

(19) Berweger, S.; Nguyen, D. M.; Muller, E. A.; Bechtel, H. A.; Perkins, T. T.; Raschke, M. B. *J. Am. Chem. Soc.* **2013**, *135*, 18292−5.

(20) Schnell, M.; Carney, P. S.; Hillenbrand, R. *Nat. Commun.* **2014**, *5*, 3499.

(21) Celik, H.; Ridge, C. D.; Shaka, A. J. *J. Magn. Reson.* **2012**, *214*, 15−21.

(22) de Beer, A. G. F.; Samson, J.-S.; Hua, W.; Huang, Z.; Chen, X.; Allen, H. C.; Roke, S. *J. Chem. Phys.* **2011**, *135*, 224701.

(23) Johansson, P. K.; Koelsch, P. *J. Am. Chem. Soc.* **2014**, *136*, 13598−13601.

(24) de Vries, R.; Briels, W.; Feil, D. *Phys. Rev. Lett.* **1996**, *77*, 1719−1722.

(25) Van Smaalen, S.; Palatinus, L.; Schneider, M. *Acta Crystallogr., Sect. A: Found. Crystallogr.* **2003**, *59*, 459−469.

(26) Vartiainen, E. M.; Rinia, H. A.; Müller, M.; Bonn, M. *Opt. Express* **2006**, *14*, 3622−3630.

(27) Hermann, P.; Hoehl, A.; Ulrich, G.; Fleischmann, C.; Hermelink, A.; Kästner, B.; Patoka, P.; Hornemann, A.; Beckhoff, B.; Rühl, E.; Ulm, G. *Opt. Express* **2014**, *22*, 17948−17958.

(28) Bechtel, H. A.; Muller, E. A.; Olmon, R. L.; Martin, M. C.; Raschke, M. B. *Proc. Natl. Acad. Sci. U. S. A.* **2014**, *111*, 7191−7196.

(29) Lerch, P.; et al. *J. Synchrotron Radiat.* **2012**, *19*, 1−9.

(30) Scarvie, T.; Andresen, N.; Baptiste, K.; Byrd, J.; Chin, M.; Martin, M. C.; McKinney, W. R.; Steier, C. *Infrared Phys. Technol.* **2004**, *45*, 403−408.

(31) Pollard, B.; Muller, E. A.; Hinrichs, K.; Raschke, M. B. *Nat. Commun.* **2014**, *5*, 3587.

(32) Moreno, T.; Westfahl, H.; de Oliveira Freitas, R.; Petroff, Y.; Dumas, P. *J. Phys.: Conf. Ser.* **2013**, *425*, 142003.

(33) Duncan, W. D.; Williams, G. P. *Appl. Opt.* **1983**, *22*, 2914−2923.

(34) Hillenbrand, R.; Knoll, B.; Keilmann, F. *J. Microsc.* **2001**, *202*, 77−83.

(35) Raschke, M. B.; Molina, L.; Elsaesser, T.; Kim, D. H.; Knoll, W.; Hinrichs, K. *ChemPhysChem* **2005**, *6*, 2197−203.

(36) Carminati, R.; Sáenz, J. *Phys. Rev. Lett.* **2000**, *84*, 5156−5159.

(37) Knoll, B.; Keilmann, F. *Opt. Commun.* **2000**, *182*, 321−328.

(38) Cvitkovic, A.; Ocelic, N.; Hillenbrand, R. *Nano Lett.* **2007**, *7*, 3177−3181.

(39) Esslinger, M.; Vogelgesang, R. *ACS Nano* **2012**, *6*, 8173−82.

(40) McLeod, A. S.; Kelly, P.; Goldflam, M. D.; Gainsforth, Z.; Westphal, A. J.; Dominguez, G.; Thiemens, M. H.; Fogler, M. M.; Basov, D. N. *Phys. Rev. B: Condens. Matter Mater. Phys.* **2014**, *90*, 085136.

(41) Govyadinov, A. A.; Amenabar, I.; Huth, F.; Carney, P. S.; Hillenbrand, R. *J. Phys. Chem. Lett.* **2013**, *4*, 1526−1531.

(42) Mastel, S.; Govyadinov, A. A.; de Oliveira, T. V. A. G.; Amenabar, I.; Hillenbrand, R. *Appl. Phys. Lett.* **2015**, *106*, 023113.

(43) Craig, I. M.; Taubman, M. S.; Lea, A. S.; Phillips, M. C.; Josberger, E. E.; Raschke, M. B. *Opt. Express* **2013**, *21*, 30401.

(44) Oyumi, Y.; Brill, T. *Combust. Flame* **1985**, *62*, 233−241.

(45) Gruzdkov, Y. A.; Gupta, Y. M. *J. Phys. Chem. A* **2001**, *105*, 6197−6202.